Waveguide nanowire superconducting single-photon detectors fabricated on GaAs and the study of their optical properties

Döndü Sahin, Alessandro Gaggero, Jan Willem Weber, Ivan Agafonov, Marcel A. Verheijen, Francesco Mattioli, Johannes Beetz, Martin Kamp, Sven Höfling (Member), Mauritius C. M. v. d. Sanden, Roberto Leoni and Andrea Fiore

(Invited paper)

***Abstract*—Quantum photonic integration is one of the leading approaches for enabling the implementation of quantum simulation and computing at the scale of tens to hundreds of photons. Quantum photonic integrated circuits (QPICs) require the monolithic integration of single-photon sources and passive circuit elements, such as waveguides and couplers, with single-photon detectors. A promising approach for *on-chip* single-photon detection is the use of superconducting nanowires on top of semiconductor waveguides. Here we present state-of-the-art NbN films on GaAs for the realization of waveguide superconducting single-photon detectors, suitable for integration with sources and linear optical circuits. Based on the measured optical properties, we propose a new design which allows high absorptance for short nanowires in order to increase the integration density in a quantum photonic chip. Finally, we review recent results on integrated single-photon and photon-number-resolving detectors, and integrated autocorrelators.**

***Index Terms*—Infrared detectors, NbN thin films, single-photon detectors, superconducting photodetectors.**

Manuscript received June 30, 2014. This work was supported in part by the Dutch Technology Foundation STW, applied science division of NWO, the Technology Program of the Ministry of Economic Affair, and the European Commission through FP7 QUANTIP (Contract No. 244026).

D. Sahin was with COBRA Research Institute, Eindhoven University of Technology, P. O. Box 513, Eindhoven 5600 MB, The Netherlands. She is now with Centre for Quantum Photonics, H. H. Wills Physics Laboratory, University of Bristol, Tyndall Avenue, Bristol, BS8 1UB, United Kingdom (e-mail: d.sahin@bristol.ac.uk)

A. Gaggero, F. Mattioli and R. Leoni are with Istituto di Fotonica e Nanotecnologie, CNR, Via Cineto Romano 42, 00156 Roma, Italy (e-mail: alessandro.gaggero@ifn.cnr.it, Francesco.mattioli@ifn.cnr.it and Roberto.leoni@ifn.cnr.it)

J.-W. Weber, I. Agafonov, Marcel A. Verheijen and A. Fiore are with Eindhoven University of Technology, P. O. Box 513, Eindhoven 5600 MB, The Netherlands (e-mail: j.w.weber@tue.nl, i.agafonov@tue.nl, m.a.verheijen@tue.nl and a.fiore@tue.nl)

J. Beetz, M. Lermer and M. Kamp are with Technische Physik, Physikalisches Institut and Wilhelm Conrad Röntgen Research Center for Complex Material Systems, Universität Würzburg, Am Hubland, D-97074 Würzburg, Germany (johannes.beetz@physik.uni-wuerzburg.de, mlermer@physik.uni-wuerzburg.de, martin.kamp@physik.uni-wuerzburg.de)

S. Höfling was with Technische Physik, Physikalisches Institut and Wilhelm Conrad Röntgen Research Center for Complex Material Systems, Universität Würzburg, Am Hubland, D-97074 Würzburg, Germany. He is now with SUPA, School of Physics and Astronomy, University of St Andrews, St Andrews, KY16 9SS, United Kingdom (sh222@st-andrews.ac.uk)

Richard M. C. M. van de Sanden is with Eindhoven University of Technology, P. O. Box 513, Eindhoven 5600 MB, The Netherlands and with Dutch Institute for Fundamental Energy Research (DIFFER), P.O. Box 1207, 3430BE Nieuwegein, The Netherlands (e-mail: M.C.M.v.d.Sanden@tue.nl)

I. Introduction

QUANTUM PHOTONICS enables the most secure form of cryptography, based on quantum key distribution (QKD) [1] as well as providing a potential platform for quantum simulation [2] and quantum computation [3]. Single-photon sources, passive circuit elements and single-photon detectors (SPDs) are the building blocks of such a platform. The practical implementation of quantum information processing (QIP) is promising for the above mentioned applications if the number of photonic quantum bits (qubits) can be increased beyond few tens [2]. It is very challenging to implement any of these quantum-processing functionalities on a large scale with bulk optics due to the extreme stability requirements as well as the complexity in size and coupling losses that scale with the number of photons. Thus, quantum photonic integration [4] is required as an approach to solve those formidable challenges by replacing bulk optics with a more compact and efficient integrated configuration in order to enable QIP beyond few tens of photons.

Many quantum optics experiments have been recently conducted with integrated passive circuit elements (optical waveguides) (see e.g. Ref. [5-8] and a review in Ref [9]). They are linked to the sources and the detectors by interfacing with fibers or in free-space. As the fabrication of 2D and 3D waveguides on silica is possible and it provides low loss in the near-infrared, it has been the most common approach for the passive circuitry [5]. Silicon and III-V materials offer a denser integration level than silica and are therefore being considered for dense quantum photonic integration [10]. In order to realize a fully-functional quantum photonic integrated circuit (QPIC), on the other hand, all the optical components are required to be integrated on a single chip [4]. The integration of single-photon detectors, such as photomultiplier tubes and single-photon avalanche photodiodes, is a challenging task due to the size and complexity. Recently, single-photon and

photon-number-resolving (PNR) detectors based on transition-edge sensors (TES) have been shown to be compatible with the integration scheme with high quantum efficiencies [11]. However, they are very slow (~µs), which limits their potential for high speed QIP, and require extremely low working temperatures. It has also been demonstrated that the superconducting single-photon detectors (SSPDs) [12] based on NbN or NbTiN nanowires can be integrated on GaAs [13-15], Si [16] and Si_3N_4 [17] waveguides. As SSPDs have been demonstrated to have high sensitivity and high efficiency [18] at telecom wavelengths, combined with their inherently short deadtime [19] and jitter [20], integrated SSPDs open the way to high-speed quantum information processing on-chip. For the realization of a fully integrated QPIC, the III-V material platform is very promising as it includes direct bandgap materials and allows the integration of single-photon sources [21]. GaAs is one of the strongest candidates amongst the heterostructures emitting in the near-infrared due to the well-developed technology for single-photon sources [21] and waveguide circuits. Moreover, GaAs provides the advantage of a second-order optical nonlinearity, useful for realizing phase modulators.

In this paper, we will first discuss the realization of state-of-the-art NbN ultrathin films (4-6 nm) on GaAs and their electrical and optical characterizations. After obtaining detailed information on the films, current and future designs of waveguide single-photon detectors (WSPDs) based on nanowires are discussed, in order to improve the efficiency. Moreover, the integration of various detection functionalities based on NbN nanowires on GaAs waveguides is reviewed, showing their potential for integration in future QPICs.

II. Methods and Concept

A. Detection Mechanism of Waveguide Single-Photon Detectors

The WSPDs exploit the same photon detection mechanism as SSPDs [12]. Upon absorption of a photon in the infrared, hundreds of Cooper pairs are broken through a relaxation of the initial quasi-particle. This perturbation of the superconducting state can lead to the formation of a resistive cross-section across the entire wire, through processes involving quasi-particle diffusion and vortices [22]. This diverts the bias current to the 50-Ω load resistance, creating a voltage pulse which is measured by standard electronics after amplification. Traditionally, the thin film, used for superconducting nanowire detectors is based on niobium nitride (NbN) due to its critical temperature, T_c well above 4K. In addition, due to high critical current, simple room temperature electronics is adequate for the signal amplification. However, inhomogeneities (or constrictions) limit the critical current of the NbN nanowires and therefore the internal efficiency and yield of the detectors [23-25]. Recently, amorphous materials such as WSi [18] and MoGe [26] have been explored. It has been shown that WSi nanowires on a cavity can reach up to >90% detection efficiency at a relatively low normalized I_b/I_c bias current, making them less sensitive to constrictions. It is very promising in terms of high yield, which allows high-density integration. On the other hand, it has also been shown for NbN that, when the nanowires are shorter as allowed by the waveguide configuration, the device quantum efficiency can increase beyond 90% [16]. This is due to the fact that shorter nanowires are less prone to having imperfections. The combination of NbN nanowires with advanced designs to maximise modal absorption, as discussed in Section IV.A, may therefore enable high efficiency and yield of WSPDs in QPICs.

B. Sputter Deposition

The fabrication of nanowire detectors is extremely challenging due to their low tolerance to variations of the nanowire properties. As a high quantum efficiency can only be obtained if the wire is biased very close to its critical current, any imperfections locally limiting the I_c strongly affects the efficiency. At the same time, the wire is extended over tens of micrometers in order to maximize the absorption [12]. This in practice requires a very uniform NbN film with thickness in the 4-5 nm range and high critical current. NbN films are deposited on GaAs substrates by a dc-magnetron reactive sputtering technique [27-28]. A 99.9 % pure, 2" Nb target is placed at the anode and argon (Ar) gas is introduced into the deposition chamber for the plasma. As the system allows low pressure sputtering owing to a highly confined plasma (magnetron sputtering), the total pressure is kept in the range of 2.0-3.0 mTorr. The concentration of the reactive gas, nitrogen (N_2) is varied between 0 and 33 % by keeping the Ar flow constant (12 sccm) in order to vary the stoichiometry of $Nb_xN_{(1-x)}$. The DC bias of 150-350 mA is applied between the anode and the cathode to provide a sufficient energy to the positive Ar ions to eject an atom from the surface of Nb target. As there are four anodes in the deposition chamber, the sample sees the Nb target under a non-zero angle and that may lead to non-uniformity in the film thickness. This is compensated by the rotation of the sample during the growth. The substrate can be heated up to 800 ºC by an infrared lamp from the back side of the substrate holder. The optimum deposition temperature is determined by varying the value between 300-600 ºC, and it is set to 410 ºC which corresponds to the lowest surface roughness and high superconducting critical temperature simultaneously [29-30].

C. Electrical and Optical Characterization Methods

The electrical properties of the films are characterized by using a dipstick in a liquid helium dewar. A wide temperature range is measured in order to determine the critical temperature (T_c), the transition width (ΔT_c) from superconducting phase to normal state and the residual resistivity ratio (RRR). The T_c and ΔT_c are determined using the average and the difference of the temperatures corresponding to 90% and 10% of the average normal resistance derived following the procedure in Ref. [27,31].

A spectroscopic ellipsometry (SE) measurement is performed using two ellipsometers working in the spectral range of 200 - 1000 nm (referred as UV-SE in the following) and of 240 - 1600 nm (referred as NIR-SE). The measurements are performed regularly with the UV-SE and only specific samples that are also studied by a high-resolution cross-sectional transmission electron microscopy (HR-XTEM)

are examined by NIR-SE in order to extract the optical constants at telecom wavelengths.

Superconducting nanowire detectors integrated on top of GaAs/AlGaAs ridge waveguides are measured using a continuous-flow helium cryogenic probe station. The devices are probed by rf, microprobes and light is coupled into the ridges by using lensed fibers (spot size of 2.5±0.5 µm at $1/e^2$). Both the probes and the fibers are located on top of XYZ piezo stages mounted on the cold plate, in order to minimize any heat load into the cryostat. Therefore, the base temperature of the cryostat can reach down to 2.1 K.

III. Superconducting Thin Film Technology

A. *Optimization of the Film Deposition*

The extreme sensitivity of the superconducting films to certain impurities during the growth requires preconditioning, which in our experiments is shown to be essential to reproducibly obtain ultrathin NbN films with high critical temperature. Before the deposition of the NbN films, Ti is sputtered in the deposition chamber and on the deposition holder to gather the oxygen [32]. After Ti pre-deposition, the base pressure is observed to decrease from 2-3x10^{-8} Torr down to 3-6x10^{-9} Torr. The positive influence of the pre-conditioning of the deposition chamber by a Ti pre-deposition is observed through the measurement of the T_c as reported in figure 1. An increase by as much as >2 K is measured in T_c with the pre-conditioning of the chamber. This is a direct measurement of the improved superconducting quality of the thin films after pre-conditioning of the deposition chamber. From the thickness scan, a deposition rate of ~ 0.6 Å/s is extracted (not shown). As the growth rate is very low, the impurity level (likely oxygen) plays a critical role in our NbN superconducting film quality.

By exploiting the pre-conditioning before every deposition run, a wide range of N_2 flows (0 – 5.9 sccm) is scanned which corresponds to 0 % up to 33 % N_2 partial pressure (12 sccm Ar gas flow). Figure 2 shows T_c, ΔT_c and RRR in the range of 8.3% to 13.3% partial pressure of N_2 for 4.0-4.6 nm-thick films. From these measurements, the optimum N_2 concentration is found to be around 10% for the thin NbN films using the deposition parameters given in Table 1. It is observed that away from the optimum concentration, the T_c decreases, possibly due to the change in the stoichiometry [27]. The ΔT_c is observed to decrease with decreasing concentration but it remains in the range of 0.55 - 0.85 K. The decrease in ΔT_c at low-N_2 concentrations may partly be due to the slightly higher film thickness (t= 4.6 nm) with respect to films grown at high concentration (t= 4.0 nm).

The RRR of NbN films on GaAs, for the optimized concentration, is below 1 as it has been observed before [27]. It has been assigned to the scattering centers at grain boundaries as the film is not single crystalline but is formed of nano-sized crystals (see figure 3). In the HR-XTEM image shown in figure 3, it is seen that there is a clear epitaxial growth of the nano-sized crystals on the substrate at the

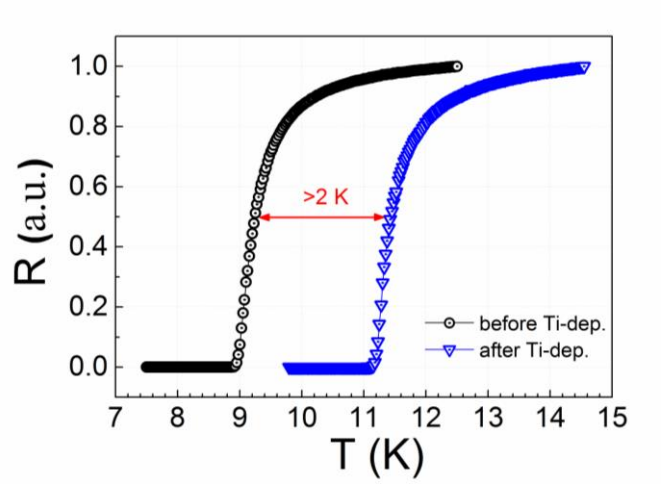

Fig. 1. Resistance curve of the 4.7 nm-thick films as a function of temperature without (black, circle) and with (blue, triangle) Ti pre-deposition in the growth chamber.

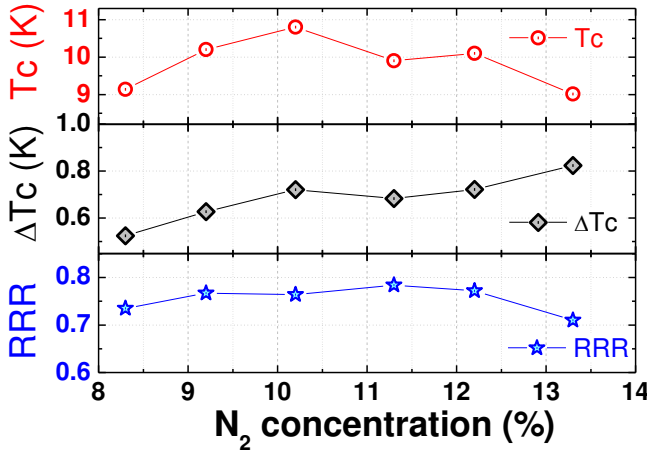

Fig. 2. Critical temperature (T_c), transition temperature (ΔT_c) and residual-resistivity-ratio (RRR) of 4.0-4.6 nm-thick films for various N_2 concentrations.

deposition temperature employed. Furthermore, the fcc NbN crystal structure is confirmed by fast-Fourier transform analysis on the data.

State-of-the-art superconducting NbN film parameters with T_c= 10.5 ± 1.0 K, ΔT_c= 0.65 ± 0.10 K and RRR= 0.81 ± 0.07 for 4-6 nm-thick films are obtained. Those values are comparable with the films grown on traditional substrates, sapphire [12] and MgO [33].

After the various deposition parameters are scanned, optimal conditions are determined and all the depositions are done with a total pressure of 2.0 mTorr accompanied by a nitrogen and argon gas flow of 1.4 sccm and 12 sccm, respectively (see Table 1). The sputter deposition system is operated at constant current mode and it is set to 250 mA. The nominal temperature during the deposition is kept at 410 ºC which provides no increase of the surface roughness as compared to the unprocessed substrate surface [28] and that is measured in the range of 0.2-0.4 nm (depending on the substrate batch) by atomic force microscopy. When the deposition voltage is kept between 345-360 V, the deposition

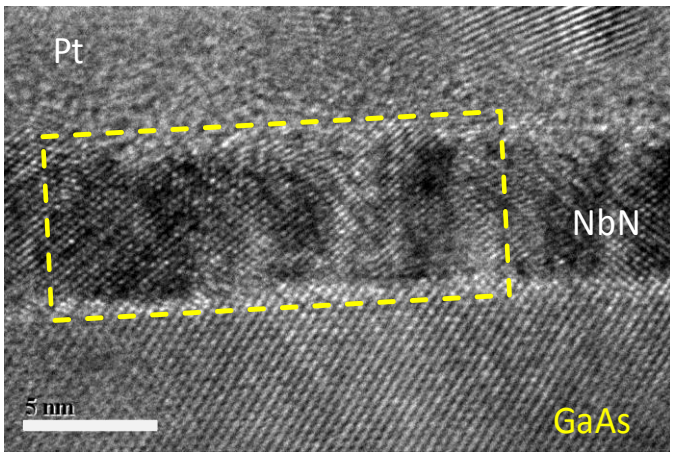

Fig. 3. A high resolution cross-sectional TEM image of a 5 nm-thick NbN film on a GaAs substrate, deposited at T= 410 ˚C. The box indicates the width of the grain.

TABLE I
OPTIMAL DEPOSITION PARAMETERS OF NbN SUPERCONDUCTING THIN FILMS

Symbol	Quantity	Optimal Parameter
T	Deposition temperature	410 ºC
N_2	Nitrogen flow	1.4 sccm
Ar	Argon flow	12 sccm
P	Deposition pressure	2.0 mTorr
I	Bias current	250 mA
V_b	Deposition voltage range	345-360 V
R	Deposition rate	~ 0.6 Å

ºC = degree Celsius, sccm = standard cubic centimeter per minute, mTorr = milli Torr, mA = milliampere, V = Volts, Å = angstrom (1.0 x 10^{-10} meter).

rate of 0.6 Å/s is obtained. Table 1 summarizes the optimal deposition parameters.

By varying the deposition time, NbN thin films in a thickness range of 2.8 - 11.0 nm are deposited on GaAs (001) substrates and the corresponding T_c values are measured. A clear trend of decreasing T_c for decreasing thickness is observed. The suppression of T_c has been studied by many groups and it has been assigned to the proximity effect, which occurs when a superconducting material is in contact with a non-superconducting layer [27,34-36]. This effect was studied in Ref. [37] and the authors found a good agreement for the thickness dependence of T_c of thin Nb films using the simplified McMillan model [38]. The McMillan model considers an inverse proximity effect in a planar thin-film geometry due to the interlayer between the superconducting and the normal layer, which reduces the electron density of states in the superconducting layer. The relation between the T_c and the thickness of the films can be calculated using the relation $T_c = T_{c0}(3.5T_D/T_{c0}\pi)^{-\alpha/d}$ [39]. In this equation, T_{c0} is the critical temperature for the bulk film (T_{c0}= 15 K), T_D= 174 K is the Debye temperature [40] and d is the film thickness. The constant $\alpha = d_N N_N(0)/N_S(0)$ where d_N is the thickness of the interlayer (presumably the inter-diffusion of elements [35]) and $N_{N,S}(0)$ are the densities of states in the normal (N) and the superconducting (S) layers at Fermi level, respectively [38]. In figure 4, the change in T_c is shown as a function of

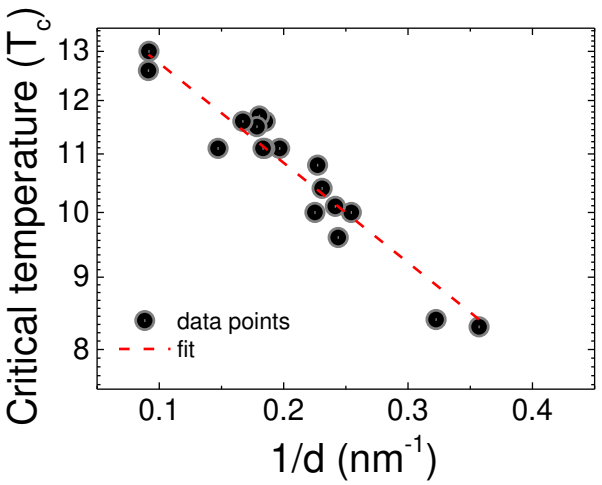

Fig. 4. The semi-log plot of critical temperature as a function of inverse thickness. The data points (black dots) are fitted by McMillian model for $d_N = \alpha = 0.63$ (red dash line).

inverse thickness in semi-log plot and clearly shows a degradation in T_c for the thin NbN films. The experimental points (black dots) are fitted (red lines) by using the MacMillan relation considering the inverse proximity effect. The fit with the McMillian model with $\alpha = 0.63 \pm 0.08$ nm (red line) is shown in figure 4. Using this value and considering $N_N(0)/N_S(0) = 1$, $d_N = \alpha = 0.63 \pm 0.08$ nm is calculated. This value is similar to the values reported for Nb [37].

B. Optical Constants of NbN Thin Films

First, in order to compare the optical constants of the NbN films grown on GaAs to the values reported in the literature for 12 nm-thick films [41], a thick film (t= 10 nm) is measured by UV ellipsometry. A complex refractive index, ñ= 3.83 - i4.39 was measured at 1000 nm for the 10 nm-thick film [30]. This result is close to the value ñ= 3.90 - i4.77 previously reported (also at 1000 nm) on a 12 nm-thick NbN film on sapphire [42]. After confirming the agreement between the thick films, this study is performed on a film, with a thickness in the range that is mostly used for the fabrication of the single-photon detectors. A thickness of $t_{SE} = 4.9 \pm 0.1$ nm has been measured by the UV-SE.

In order to confirm the thickness obtained by SE, an HR-XTEM analysis has been conducted for the thin film. The HR-XTEM measurement validates a thickness of $t_{TEM} = 5.2 \pm 0.2$ nm. As the two measurements are in relatively good agreement, the NIR-SE measurement is performed on the same sample in order to also extract the optical constants at 1310 nm and 1550 nm. For the NIR-SE measurement, the thickness is fixed to the value determined by UV-SE and used to get the optical constant for the near-infrared range of the spectrum. Figure 5 shows the real (n) and imaginary (k) parts of the dielectric constant (ñ = n - ik) measured by both UV-SE and NIR-SE as a function of wavelength for the 4.9 nm-thick NbN film on GaAs (001) (fitted by the B-spline model [43]). There is a small discrepancy for n between two measurements. However, at the measurement angle (75º), the UV-SE is more sensitive at short wavelengths while the NIR-SE becomes more sensitive at long wavelengths. Therefore, we confirmed

that reporting the thickness by UV-SE and the optical constants by NIR-SE is a reliable approach. The complex refractive indices at telecom wavelengths are reported in the Table 2. The value at 1550 nm is lower as compared to the one reported in Ref. [41] for a 12 nm-thick film on sapphire (ñ =5.23 – i5.82), which has been used in the literature in order to simulate the detector structures, including the detectors on GaAs. However, our results show a better agreement with the values reported in Ref. [44] for 9 nm-thick films on silica (ñ = 4.91 – i4.29). The difference in optical constants is assigned to the difference in thicknesses as well as tentatively to the different substrates and also to the deposition temperature (set by the substrate), which may be responsible for the material properties.

IV. Waveguide Superconducting Single Photon Detectors (WSPDs)

A. *Design*

We analyze two designs to realize SSPDs on an integrated platform. They are based on 5 nm-thick and 80 - 100 nm-wide nanowires on top of either GaAs waveguides or nanobeams.

The first design was used in the first demonstration of a WSPD with an NbN meander (5 nm-thick, 100 nm-wide and nanowire with a 250 nm-pitch) placed on top of a GaAs (300 nm)/$Al_{0.7}Ga_{0.3}As$ waveguide [13]. There is about 100 nm electron beam resist remaining on top of the nanowire after processing, which is a form of amorphous silicon oxide. Therefore, we simulate that as a SiO_x in our design. Figure 6 (a) shows the sketch of nanowire detectors on top of the GaAs/AlGaAs waveguide heterostructure. A 1.85 μm-wide and 250 nm-deep ridge is etched to provide the 2D confinement in the photonic waveguide. For this design, if we use the refractive index of NbN, GaAs, AlGaAs and SiO_2, $\tilde{n}_{NbN}$ = 4.35 – i4.65 nm, $\tilde{n}_{GaAs}$ = 3.39, $\tilde{n}_{AlGaAs}$ = 3.07 and $\tilde{n}_{SiOx}$ = 1.46 at 1310, modal absorption coefficients of α_{abs}^{TE} = 370 cm^{-1} and α_{abs}^{TM} = 347 cm^{-1} are calculated for TE and TM polarizations, respectively at λ= 1310 nm by using a finite element mode solver. The absorption coefficients for TE and TM polarizations provide a total absorptance (A) of 84% and 82% for a 50 μm-long waveguide, respectively. The design provides a high absorptance due to the large overlap of the electric field with the nanowires, as shown by the simulated electric field distribution of the fundamental TE mode in figure 7(left). While this waveguide supports both quasi-TE and -TM modes, the quasi-TM mode has a complex distribution of electric field polarization which makes coupling of TM-polarized light to the waveguide inefficient (see supplementary document). This is, however, not a problem for QPICs on GaAs as InAs quantum dots in waveguides emit in the TE polarization.

In addition, if the GaAs core layer thickness is increased by 50 nm to 350 nm, the complex distribution of electric field in quasi-TM mode disappears [45] and nearly polarization-independent devices are obtained. This design modifies the modal absorption for both polarizations (α_{abs}^{TE} = 313 cm^{-1} and α_{abs}^{TM} = 391 cm^{-1}), and maintains a high absorptance A_{TE} = 79%, A_{TM} = 86% for 50 μm-long waveguide detectors. While the theoretical calculations suggest a high absorptance, NbN nanowires suffer from inhomogeneities [23-24], which limit their efficiency and yield. As the short nanowires have a lower probability of having constrictions, they result in high efficiency as demonstrated in Ref [16].

TABLE II
Optical constants of 4.9 nm-thick NbN on top of GaAs substrate

Refractive index	1310 nm	1550 nm
n	4.35	4.93
k	4.65	4.86

n = real part of the refractive index, k = imaginary part of the refractive index, nm = nanometer (1.0 x 10^{-9} meter)

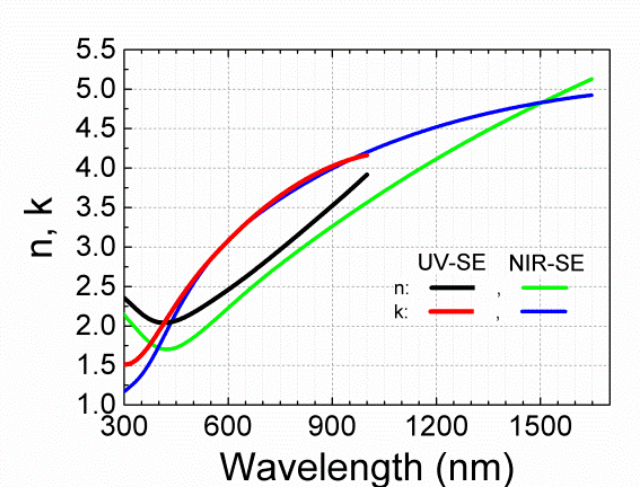

Fig. 5. Wavelength dependent optical constants of 4.9 nm-thick NbN films on a GaAs substrate, measured by UV-SE (black and red lines) and NIR-SE (green and blue lines).

Thus, here a new design for WSPDs on GaAs is proposed as a possible improvement. In this design (Figure 6 (b)), one NbN nanowire is folded in a meander shape (5 nm-thick, 80 nm wide wires with a 250 nm-pitch) on top of a 500 nm-wide and 300 nm-thick GaAs suspended nanobeam surrounded by air (see Ref. [46]). As the index contrast between GaAs and the bottom cladding layer is higher as compared to the previous design, the field is pushed towards the top GaAs/NbN interface and the absorptance is improved for the TE and especially for the TM polarization. The modal absorption coefficients for TE and TM polarizations at 1310 nm are calculated as α_{abs}^{TE} = 957 cm^{-1} and α_{abs}^{TM} = 3151 cm^{-1}, respectively by using $\tilde{n}_{NbN}$ = 4.35 – i4.65. The corresponding fundamental TE mode is presented in Figure 7(right). As shown in figure 8, 90% of the infrared input light will be absorbed by the NbN nanowires in a 24 μm-long nanobeam for the TE polarisation and in a nanobeam as short as 7 μm for the TM polarization. This nanobeam structure may also be suitable for the integration of a quantum-dot based single-photon source. Efficient coupling between nanobeams and ridge waveguide is also possible [46].

As very high internal efficiency has been demonstrated with a low bandgap material, WSi, we have also calculated the absorptance of a WSi nanowire (5 nm-thick, 150 nm-wide

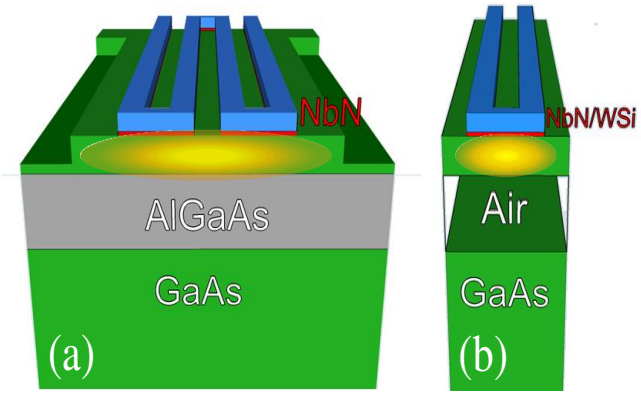

Fig. 6. Schematics of a NbN superconducting nanowire on (a) a GaAs/AlGaAs ridge waveguide and (b) a GaAs nanobeam (The materials are color coded, Green: GaAs, red: NbN or WSi nanowire, grey: AlGaAs and blue is SiO_x).

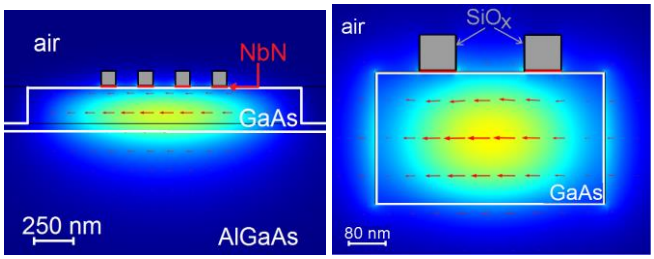

Fig. 7. The simulated electric field distribution of the fundamental TE mode for NbN nanowire on top of (left) a GaAs (300 nm)/AlGaAs ridge waveguide and (right) a GaAs nanobeam. In both figures, GaAs is shown inside a white contour, NbN nanowires are colored in red and SiO_x in grey.

with 250 nm pitch length) as in Ref. [18]) on the nanobeam. The modal absorption coefficients α_{abs}^{TE} = 1333 cm^{-1} and α_{abs}^{TM} = 3810 cm^{-1} are calculated for TE and TM polarized light, respectively by using the refractive index $\tilde{n}_{WSi}$ = 4.35 – i3.38 from Ref. [18]. That allows 90% absorptance along 17 μm-long nanobeam for the TE polarization and 6 μm-long nanobeam for the TM polarization.

Figure 8 compares the absorptance along the nanowires for two different designs, on top of a ridge waveguide and a nanobeam. The absorptance calculated for NbN nanowires on the suspended nanobeam is higher as compared to ridge waveguides, corresponding to the larger overlap of the mode with the nanowires (mainly related to the lower index of the cladding). On the other hand, on the nanobeam structure, the WSi nanowire absorbs a larger portion of the field at a shorter length as it has a larger cross section than NbN nanowire.

B. Fabrication

Superconducting nanowire WSPDs are fabricated on top of a GaAs (300 nm or 350 nm) /$Al_{0.75}Ga_{0.25}As$ (1.5 μm) heterostructure grown by molecular beam epitaxy on an undoped GaAs (001) substrate. A 4-6 nm-thick NbN layer is deposited by dc reactive magnetron sputtering of a Nb target in a N_2/Ar plasma, with deposition parameters optimized for GaAs substrates as described above and in Ref. [28], resulting in a T_c= 9.5-11.5 K. There are four steps of direct-writing 100 kV electron beam lithography (EBL) for the fabrication of the WSPDs. First, the electrical contact pads (Ti(10 nm)/Au(60

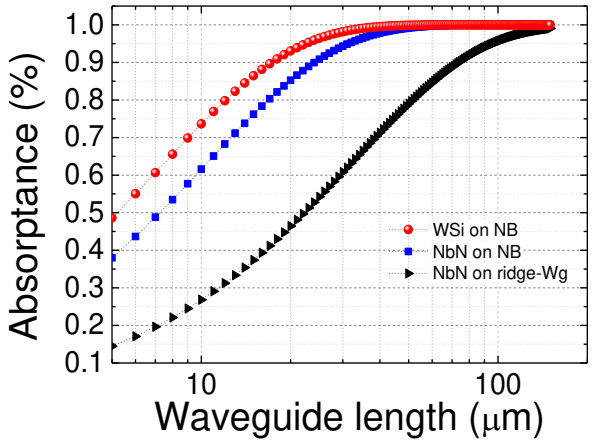

Fig. 8. Absorptance for TE polarized light at 1310 nm is calculated for a NbN nanowire on a GaAs (350 nm)/AlGaAs ridge waveguide (triangle), for a NbN nanowire on GaAs (300 nm-thick) nanobeam (NB, square) and for a WSi nanowire on GaAs (300 nm-thick) nanobeam (NB, sphere). The refractive index of NbN is $\tilde{n}_{NbN}$ = 4.35 - i4.65 and WSi is $\tilde{n}_{WSi}$ = 4.35 – i3.38.

nm) and alignment markers are fabricated by electron beam evaporation and lift-off using a polymethylmethacrylate (PMMA) stencil mask. Second, the meander nanowire (100nm-wide and 30-100 μm-long nanowires with 250nm pitch) is defined on a 180 nm thick hydrogen silsesquioxane (HSQ) mask and then transferred to the NbN film with a (CHF_3+SF_6+Ar) reactive ion etching (RIE). In the third step, an HSQ-mask is patterned by carefully realigning this layer with the previous one in order to define 1.85 μm-wide waveguides. This layer also protects the Ti/Au pads against the subsequent reactive etching process. Successively, 250-300 nm of the underlying GaAs layer is etched by a Cl_2+Ar ECR (electron cyclotron resonance) RIE to obtain a ridge waveguide. Finally, holes are opened through the remaining HSQ-mask, for the electrical wiring to the TiAu pads, using a PMMA mask and RIE in a CHF_3 plasma.

Waveguide photon-number-resolving detectors require two extra EBL steps for the parallel integrated resistors [47]. First, electrical connection pads (Ti(5nm)/Au(20nm)) for the parallel resistors are written and lift-offed by using polymethyl methacrylate as second step before patterning of the nanowires on HSQ. The AuPd resistors, on the other hand, are defined right before the waveguide mask patterning. The Ti(10 nm)/AuPd(50 nm) resistors are fabricated by lift-off using a PMMA stencil mask. Each resistor is 500 nm wide and 3.5 μm long corresponding to a design value of R_p= 49 Ω. The inset in figure 11 shows the sketch of parallel resistances.

C. Results and Discussions

WSPDs integrated with GaAs ridge waveguides were reported recently by us and other groups, [13,15,45, 47-48] and the main results of our work are summarized here. There are two ways of reporting the quantum efficiency (QE) of the detectors. The first one is the system quantum efficiency (SQE). The SQE is the probability that the detector clicks if a photon is incident at the input of the detection system. The SQE in our experiments is obtained by dividing the number of

counts by the number of photons at the fiber input of the cryostat. The second relevant efficiency parameter is the device quantum efficiency (DQE), which is defined as the number of counts divided by the number of photons coupled in the waveguide and does not include the waveguide coupling losses. The DQE is directly related to the material and the geometry of the detector. The DQE is not setup dependent (as long as the operating temperature is kept the same). The SQE and the DQE are related and the SQE is equal to the product of the DQE and the coupling efficiency (η_c) of the light to the waveguide, SQE= DQExη_c. The coupling efficiency for the ridge waveguide design (see Fig. 6(a)) is measured to be $\eta_c^{TE} \approx 17$ % using the method described in the Supplementary text. The waveguide losses are estimated to be negligible for our GaAs/AlGaAs ridge waveguides. We note that the DQE is the most relevant figure of merit for integrated applications as all the optical components will be integrated on chip.

WSPDs are fabricated on 50 µm-long ridge waveguides with a 300 nm-thick GaAs core, which allows 90% absorptance. A critical current of 16.9 µA is reported [13] and at its maximum bias current (I_b~I_c), we have demonstrated that the DQE of a WSPD for TE polarized input light at 1310 nm reaches ~20 % as shown in figure 9. The difference between the calculated absorptance and the experimental DQE is attributed to the limited internal QE (probability that the detector clicks after a photon is absorbed). These WSPDs have a timing jitter of ~60 ps and a dead time of a few ns (see inset of figure 9) [13]. While coupling TM-polarized light to these WSPDs is inefficient due to the design (as discussed in the design section), polarization-independent detectors have also been demonstrated by increasing the thickness of the GaAs core by 50 nm [45]. The dark count rate (DCR) was also measured (not shown) and presents the usual exponential dependence as a function of the bias current [13], being comparable to the DCR measured on SSPDs.

Taking advantage of the waveguide geometry, a more advanced functionality is realized by integrating an intensity autocorrelator on a single ridge waveguide. Such waveguide autocorrelator [45] consists of two electrically-distinct nanowires patterned on top of the same ridge waveguide (see inset in figure 10). Similar to the conventional Hanbury-Brown and Twiss set-up, realized with a beam splitter and two single-photon detectors, the correlation of the detector outputs allows measuring the second-order intensity correlation function, $g^{(2)}(\tau)$. The two detectors in the waveguide autocorrelator reach very similar efficiencies at high bias current, as shown in figure 10. We also checked for the possible existence of cross-talk (spurious interaction between the two detectors on a waveguide). For that purpose, the coincidence counts of continuous wave and pulsed light sources have been measured and no crosstalk is evidenced within our experimental accuracy (~ 4%) [45]. The inset of figure 10 shows a correlation trace measured on a CW laser, showing the absence of peaks or dips at zero delay, which would indicate cross-talk. These autocorrelators have a temporal resolution of 125 ps, including the jitter of both detectors and of the electronics. They provide a high temporal resolution with a very compact configuration for on-chip measurements of the second-order correlation function.

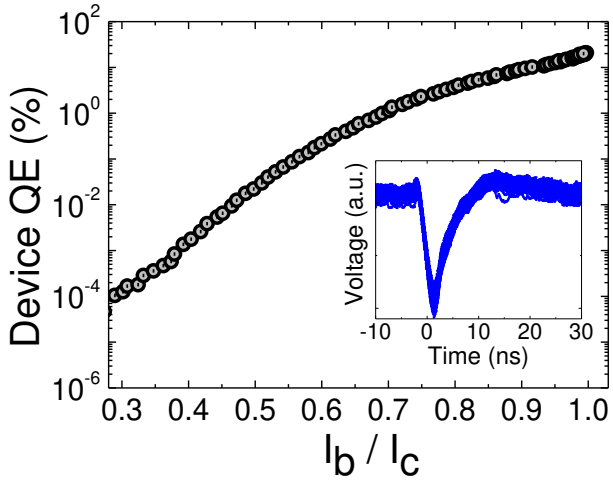

Fig. 9. Device quantum efficiency (QE) of a WSPD based on GaAs (300 nm)/AlGaAs (1.5 µm) for TE polarization at 1310 nm. Inset: Electrical output pulse of a NbN nanowire WSPD.

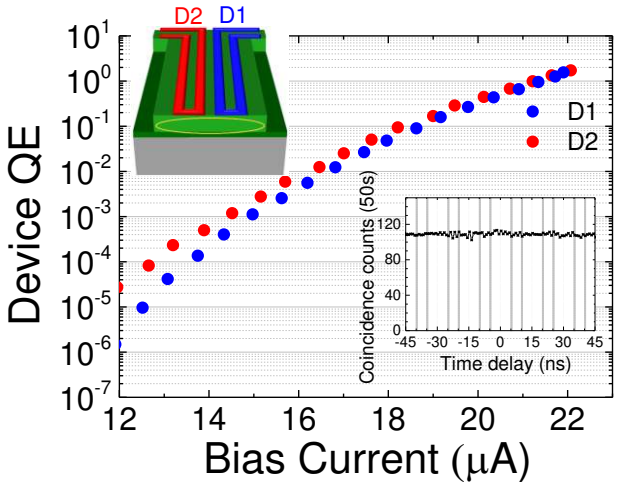

Fig. 10. Device QE of two adjacent detectors (two WSPDs) on top of GaAs (350 nm)/AlGaAs (1.5 µm) for a polarization independent design. Inset: The second-order intensity correlation measurement at I_b=0.99xI_c. Both measurements are conducted with a laser diode operating at 1310 nm.

Finally, a waveguide photon-number-resolving detector (WPNRD) was demonstrated on a GaAs ridge waveguide [14]. It is based on the series connection of four nanowires patterned on the same ridge waveguide (see inset of figure 11), following the series-nanowire concept proposed in Ref. [49]. The inset of figure 12 depicts the equivalent circuit of the WPNRDs. Each nanowire is modeled with a switch, which opens upon photon absorption, and a normal resistance connected in series with a kinetic inductance. Each wire is connected to a parallel integrated resistor and four of these wires are connected in series. Upon absorption of a single photon in one wire the corresponding bias current is diverted to the parallel resistance, producing a voltage pulse at the output. If more photons are absorbed in different wires, the corresponding voltages are summed up, producing a signal proportional to the number of photons [49-50]. As shown in figure 11, in this WPNRD a single-photon device quantum efficiency of ~24 % (22%) has been reported for TE (TM) polarized light at 1310 nm in the single photon detection regime with an estimated maximum count rate of >50 MHz.

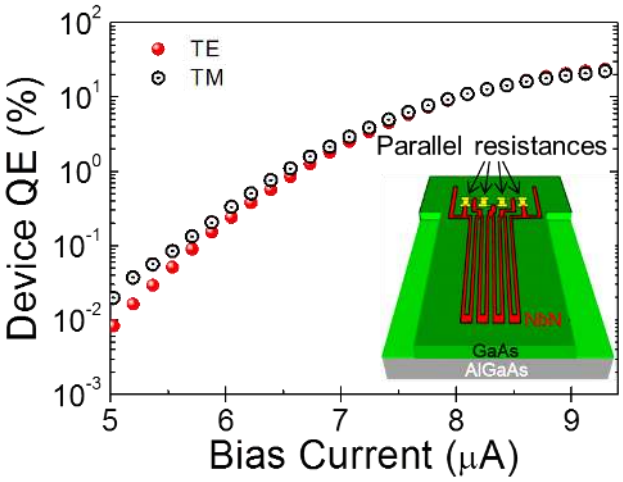

Fig. 11. Device QE of a WPNRD. The measurements are done with a diode laser working at 1310 nm. Inset: Schematic of the device: Each nanowire (red) is connected in parallel to a shunt resistor (yellow) and four wires are connected in series.

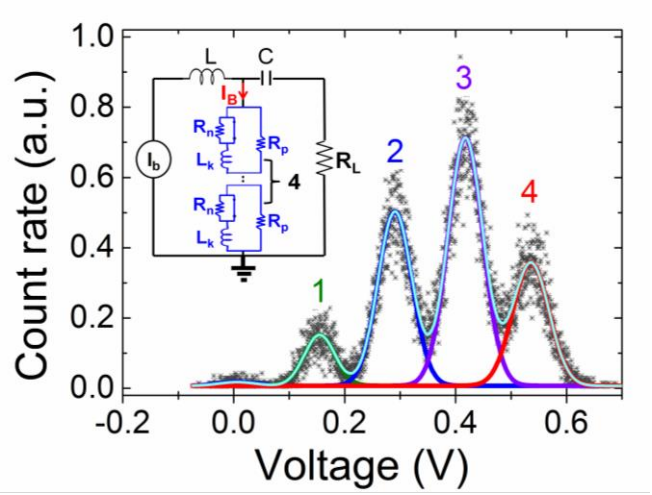

Fig. 12. A histogram with multi-Gaussian fit (cyan) of a WPNRD signal for a flux of 16 photons/pulse in the waveguide. The distinct detection levels with 1- (green), 2- (blue), 3- (purple) and 4- (red) photon levels are shown. Inset: Equivalent circuit of a WPNRD. L: Inductance and C: capacitance of bias tee, R_n: normal resistance, L_k: kinetic inductance of nanowires and R_p: integrated parallel resistance, R_L: load resistance.

The PNR functionality was observed [14], as shown from the clearly distinct output levels in the oscilloscope trace in figure 12. The figure presents a histogram of the amplitude of the detector output pulses, at a bias current of 8.8 μA, when illuminated with laser pulses with an average photon number of 2.9/pulse in the waveguide and a repetition rate of 2 MHz. The voltage peaks, corresponding to 1-4 photon levels, are nearly equally spaced with a small increase in the noise which has been extensively discussed in Ref. [14]. The PNR measurement fidelity in this design is partly limited by the difference in absorptance on the nanowires depending on their position on the waveguide. This results from the single mode profile in a waveguide, which has a higher intensity at the center with correspondingly higher absorptance in the central nanowires. This, however, can be overcome by adiabatically converting the single mode to multi modes to modify the mode profile such that the absorptance by the all wires will be equal. The high timing resolution and count rate, and relatively high operation temperature make these WPNRDs attractive as compared to waveguide TESs, which also show photon number resolving ability [11].

V. Conclusion

In summary, we presented a fabrication method and characterization results of ultrathin NbN superconducting films on GaAs for the realization of integrated single-photon and photon-number-resolving detectors for applications in quantum photonic integration circuits. The design of WSPDs is discussed, including a new design based on a GaAs nanobeam which is anticipated to overcome the limited device quantum efficiency due to constrictions along the nanowire.

WSPDs based on NbN nanowires on GaAs ridge waveguides are presented with 20% device quantum efficiency. They show low jitter and short dead time in the few ns range. Furthermore, polarization-independent integrated autocorrelators are demonstrated and the $g^{(2)}(\tau)$ measurement of a continuous wave laser is shown as a proof of concept. No crosstalk is evidenced between two closely packed nanowires on a waveguide. Finally, WPNRDs are presented based on four NbN nanowires, which can resolve up to four-photons in an input pulse. They show a DQE of 24% for TE polarization and have a maximum estimated count rate of >50 MHz.

Acknowledgment

The authors would like to thank J.P. Sprengers, S. Jahanmirinejad, Z. Zhou and M. Lermer for experimental assistance and helpful discussions.

REFERENCES

[1] Gisin N., Ribordy G. and Zbinden H. "Quantum cryptography" Reviews of Modern Physics 74 (1), 145-195 (2002)

[2] Aspuru-Guzik, A., and Walther, P. "Photonic quantum simulators" Nature Physics, 8(4), 285-291 (2012)

[3] Ladd, T. D., Jelezko, F., Laflamme, R., Nakamura, Y., Monroe, C., and O'Brien, J. L. "Quantum computers" Nature, 464(7285), 45-53 (2010).

[4] O'Brien, J. L., Furusawa, A., and Vučković, J. "Photonic quantum technologies" Nature Photonics, 3(12), 687-695 (2009).

[5] Politi, A., Cryan, M. J., Rarity, J. G., Yu, S., and O'Brien, J. L. "Silica-on-silicon waveguide quantum circuits" Science, 320(5876), 646-649 (2008).

[6] Peruzzo, A., Lobino, M., Matthews, J. C., Matsuda, N., Politi, A., Poulios, K., Zhou X.-Q., Lahini Y., Ismail N., Wörhoff K., Bromberg Y., Silberberg Y., Thompson M. G. and O'Brien, J. L. "Quantum walks of correlated photons" Science, 329(5998), 1500-1503 (2010).

[7] Metcalf, B. J., Thomas-Peter, N., Spring, J. B., Kundys, D., Broome, M. A., Humphreys, P. C., Jin X.-M., Barbieri M., Kolthammer W. S., Gates J. C., Smith B. J., Langford N. K., Smith P. G. R and Walmsley, I. A. "Multiphoton quantum interference in a multiport integrated photonic device" Nature Communications, 4, 1356 (2013).

[8] Crespi, A., Osellame, R., Ramponi, R., Brod, D. J., Galvão, E. F., Spagnolo, N., Vitelli C., Maiorino E., Mataloni P. and Sciarrino, F. "Integrated multimode interferometers with arbitrary designs for photonic boson sampling" Nature Photonics, 7(7), 545-549 (2013).

[9] Tanzilli, S., Martin, A., Kaiser, F., De Micheli, M. P., Alibart, O., & Ostrowsky, D. B. "On the genesis and evolution of integrated quantum optics" Laser & Photonics Reviews, 6(1), 115-143 (2012).

[10] Bonneau, D., Engin, E., Ohira, K., Suzuki, N., Yoshida, H., Iizuka, N., Ezaki M., Natarajan C. M., Tanner M. G., Hadfield R. H., Dorenbos S. N., Zwiller V., O'Brien J. L. and Thompson, M. G. "Quantum interference and manipulation of entanglement in silicon wire waveguide quantum circuits" New Journal of Physics, 14(4), 045003 (2012).

[11] Gerrits, T., Thomas-Peter, N., Gates, J. C., Lita, A. E., Metcalf, B. J., Calkins, B., Tomlin N. A., Fox A. E., Linares A. L., Spring J. B., Langford N. K., Mirin R. P., Smith P. G. R., Walmsley I. A. and Nam, S. W. "On-chip, photon-number-resolving, telecommunication-band detectors for scalable photonic information processing" Physical Review A, 84(6), 060301 (2011).

[12] Gol'Tsman, G. N., Okunev, O., Chulkova, G., Lipatov, A., Semenov, A., Smirnov, K., Voronov B., Dzardanov A., Williams C., and Sobolewski, R. "Picosecond superconducting single-photon optical detector" Applied Physics Letters, 79(6), 705-707 (2001).

[13] Sprengers, J. P., Gaggero, A., Sahin, D., Jahanmirinejad, S., Frucci, G., Mattioli, F., Leoni R., Beetz J., Lermer M., Kamp M., Höfling S., Sanjines R. and Fiore, A. "Waveguide superconducting single-photon detectors for integrated quantum photonic circuits" Applied Physics Letters, 99(18), 181110 (2011).

[14] Sahin, D., Gaggero, A., Zhou, Z., Jahanmirinejad, S., Mattioli, F., Leoni, R., Beetz J., Lermer M., Kamp M., Höfling S., and Fiore, A. "Waveguide photon-number-resolving detectors for quantum photonic integrated circuits" Applied Physics Letters, 103(11), 111116 (2013).

[15] Reithmaier, G., Lichtmannecker, S., Reichert, T., Hasch, P., Müller, K., Bichler, M., Gross R., and Finley, J. J. "On-chip time resolved detection of quantum dot emission using integrated superconducting single photon detectors" Scientific Reports, 3 (2013).

[16] Pernice, W. H. P., Schuck, C., Minaeva, O., Li, M., Goltsman, G. N., Sergienko, A. V., and Tang, H. X. "High-speed and high-efficiency travelling wave single-photon detectors embedded in nanophotonic circuits" Nature Communications, 3, 1325 (2012).

[17] Schuck, C., Pernice, W. H., and Tang, H. X. "Waveguide integrated low noise NbTiN nanowire single-photon detectors with milli-Hz dark count rate" Scientific Reports, 3 (2013).

[18] Marsili F., Verma V. B., Stern J. A., Harrington S., Lita A. E., Gerrits T., Vayshenker I., Baek B., Shaw M. D., Mirin R. P., Nam S. W. "Detecting single infrared photons with 93 % system efficiency" Nature Photonics, 7(3), 210-214 (2013).

[19] Kerman, A. J., Yang, J. K., Molnar, R. J., Dauler, E. A., and Berggren, K. K. "Electrothermal feedback in superconducting nanowire single-photon detectors" Physical Review B, 79(10), 100509 (2009).

[20] Dauler, E. A., Kerman, A. J., Robinson, B. S., Yang, J. K., Voronov, B., Goltsman, G., Hamilton, S. A. and Berggren, K. K. "Photon-number-resolution with sub-30-ps timing using multi-element superconducting nanowire single photon detectors" Journal of Modern Optics 56(2-3), 364-373 (2009).

[21] Shields, A. J. "Semiconductor quantum light sources" Nature Photonics, 1(4), 215-223 (2007).

[22] Renema, J.J., Gaudio, R., Wang, Q., Zhou, Z., Gaggero, A., Mattioli, F., Leoni, R., Sahin, D., de Dood, M.J.A., Fiore, A. and van Exter M.P. "Experimental Test of Theories of the Detection Mechanism in a Nanowire Superconducting Single Photon Detector" Physical Review Letters 112(11), 117604 (2014)

[23] Kerman, A. J., Dauler, E. A., Yang, J. K., Rosfjord, K. M., Anant, V., Berggren, K. K., Gol'tsman G. N. and Voronov, B. M. Constriction-limited detection efficiency of superconducting nanowire single-photon detectors. Applied Physics Letters, 90(10), 101110 (2007).

[24] Hadfield, R. H., Dalgarno, P. A., O'Connor, J. A., Ramsay, E., Warburton, R. J., Gansen, E. J., Baek B., Stevens M. J., Mirin R. P. and Nam, S. W. "Submicrometer photoresponse mapping of nanowire superconducting single-photon detectors" Applied Physics Letters, 91(24), 241108 (2007).

[25] F. Mattioli, R. Leoni, A. Gaggero, M. G. Castellano, P. Carelli, F. Marsili and A. Fiore. "Electrical characterization of superconducting single-photon detectors" Journal of Applied Physics, 101 (5) 054302 (2007).

[26] Verma, V. B., Lita, A. E., Vissers, M. R., Marsili, F., Pappas, D. P., Mirin, R. P. and S. W. Nam "Superconducting nanowire single photon detectors fabricated from an amorphous $Mo_{0.75}Ge_{0.25}$ thin film." arXiv:1402.4526 (2014).

[27] Marsili, F., Gaggero, A., Li, L. H., Surrente, A., Leoni, R., Lévy, F., and Fiore, A. "High quality superconducting NbN thin films on GaAs" Superconductor Science and Technology, 22(9), 095013 (2009).

[28] Gaggero, A., Nejad, S. J., Marsili, F., Mattioli, F., Leoni, R., Bitauld, D., Sahin D., Hamhuis G. J., Nötzel R., Sanjines R. and Fiore, A. "Nanowire superconducting single-photon detectors on GaAs for integrated quantum photonic applications" Applied Physics Letters, 97(15), 151108 (2010).

[29] Guillén-Cervantes, A., Rivera-Alvarez, Z., Lopez-Lopez, M., Lopez-Luna, E., and Hernández-Calderón, I. "GaAs surface oxide desorption by annealing in ultra high vacuum" Thin Solid Films, 373(1), 159-163 (2000).

[30] Sahin D. "Waveguide single-photon and photon-number-resolving detectors" Doctoral dissertation, Eindhoven University of Technology (2014)

[31] Marsili, F. "Single-photon and photon-number-resolving detectors based on superconducting nanowires" Doctoral dissertation, École Polytechnique Fédérale De Lausanne (2009).

[32] Ti pre-deposition provides improvement in the base pressure by decomposing the water molecules and forming TiO_2, as known from the working principle of the Ti-sublimation pumps.

[33] Marsili, F., Bitauld, D., Fiore, A., Gaggero, A., Mattioli, F., Leoni, R., Benkahoul M., and Lévy, F. "High efficiency NbN nanowire superconducting single photon detectors fabricated on MgO substrates from a low temperature process" Optics Express, 16(5), 3191-3196 (2008).

[34] Cooper, L. N. "Superconductivity in the neighborhood of metallic contacts" Phys. Rev. Letters, 6(12), 689 (1961).

[35] Ilin, K., Schneider, R., Gerthsen, D., Engel, A., Bartolf, H., Schilling, A., Semenov A., Huebers H.-W., Freitag B., and Siegel, M. "Ultra-thin NbN films on Si: crystalline and superconducting properties" IOP Publishing, Journal of Physics: Conference Series, 97(1) (2008).

[36] Zhang, J. J., Su, X., Zhang, L., Zheng, L., Wang, X. F., and You, L. "Improvement of the superconducting properties of NbN thin film on single-crystal silicon substrate by using a TiN buffer layer" Superconductor Science and Technology, 26(4), 045010 (2013).

[37] Delacour, C., Ortega, L., Faucher, M., Crozes, T., Fournier, T., Pannetier, B., and Bouchiat, V. "Persistence of superconductivity in niobium ultrathin films grown on R-plane sapphire" Physical Review B, 83(14), 144504 (2011).

[38] McMillan, W. L. "Tunneling model of the superconducting proximity effect" Physical Review, 175(2), 537 (1968).

[39] Ezaki, S., Makise, K., Shinozaki, B., Odo, T., Asano, T., Terai, H., Yamashita T., Miki S. and Wang, Z. "Localization and interaction effects in ultrathin epitaxial NbN superconducting films" Journal of Physics: Condensed Matter, 24(47), 475702 (2012).

[40] Chockalingam, S. P., Chand, M., Jesudasan, J., Tripathi, V., and Raychaudhuri, P. "Superconducting properties and Hall effect of epitaxial NbN thin films" Physical Review B, 77(21), 214503 (2008).

[41] Anant, V., Kerman, A. J., Dauler, E. A., Yang, J. K., Rosfjord, K. M., and Berggren, K. K. “Optical properties of superconducting nanowire single-photon detectors” Optics Express, 16(14), 10750-10761 (2008).
[42] Anant, V. “Engineering the optical properties of subwavelength devices and materials” Doctoral dissertation, Massachusetts Institute of Technology (2007).
[43] Weber, J. W., Hansen, T. A. R., Van de Sanden, M. C. M., and Engeln, R. “B-spline parametrization of the dielectric function applied to spectroscopic ellipsometry on amorphous carbon” Journal of Applied Physics, 106(12), 123503 (2009).
[44] Yamashita, T., Miki, S., Terai, H. and Wang, Z. “Low-filling-factor superconducting single photon detector with high system detection efficiency” Optics Express 21(22), 27177-27184 (2013).
[45] Sahin, D., Gaggero, A., Hoang, T. B., Frucci, G., Mattioli, F., Leoni, R., Beetz J., Lermer M., Kamp M., Höfling S., and Fiore, A. “Integrated autocorrelator based on superconducting nanowires” Optics express, 21(9), 11162-11170 (2013).
[46] Fattah Poor, S., Hoang, T. B., Midolo, L., Dietrich, C. P., Li, L. H., Linfield, E. H., Schouwenberg, J. F. P., Xia, T., Pagliano F. M. and Fiore, A. “Efficient coupling of single photons to ridge-waveguide photonic integrated circuits” Applied Phyics. Letters 102(13), 131105 (2013).
[47] Ghamsari B. G. and Majedi A. H. “Theory of superconductive travelling-wave detectors” IEEE Transaction on Applied Superconductivity 18(4), 1761-1768 (2008).
[48] Xiaolong H., Holzwarth, C.W., Masciarelli, D., Dauler, E.A. and Berggren, K.K. “Efficiently coupling light to superconducting nanowire single-photon detectors” IEEE Transaction on Applied Superconductivity 19(3), 336-340 (2009).
[49] Jahanmirinejad S. and Fiore A. “Proposal for a superconducting photon number resolving detector with large dynamic range” Optics Express 20(5), 5017-5028 (2012).
[50] Jahanmirinejad S., Frucci G., Mattioli F., Sahin D., Gaggero A., Leoni R., and Fiore A. “Photon-number resolving detector based on a series array of superconducting nanowires” Applied Physics Letters 101(7), 072602 (2012).